The Astrophysical Journal, 757:44 (14pp), 2012 September 20 doi:10.1088/0004-637X/757/1/44

COSMIC MICROWAVE BACKGROUND INDUCED POLARIZATION FROM SINGLE SCATTERING BY CLUSTERS OF GALAXIES AND FILAMENTS

Elsa P. R. G. Ramos[1,2], António J. C. da Silva[1], and Guo-Chin Liu[3]
[1] Centro de Astrofísica, Universidade do Porto, Rua das Estrelas, 4150-762 Porto, Portugal; eramos@astro.up.pt
[2] Departamento de Física e Astronomia, Faculdade de Ciências, Universidade do Porto, Rua do Campo Alegre, 4169-007 Porto, Portugal
[3] Department of Physics, Tamkang University, Tamsui District, New Taipei City 251, Taiwan, Republic of China
Received 2012 June 13; accepted 2012 July 25; published 2012 September 4

ABSTRACT

We present light-cone-integrated simulations of the cosmic microwave background (CMB) polarization signal induced by a single scattering in the direction of clusters of galaxies and filaments. We characterize the statistical properties of the induced polarization signals from the presence of the CMB quadrupole component (pqiCMB) and as the result of the transverse motion of ionized gas clouds with respect to the CMB rest frame (pβ_t^2SZ). From adiabatic *N*-body/hydrodynamic simulations, we generated 28 random sky patches integrated along the light cone, each with about 0.86 deg^2 and angular resolution of $6''$. Our simulation method involves a box-stacking scheme that allows to reconstruct the CMB quadrupole component and the gas physical properties along the line of sight. We find that the linear polarization degree in the logarithmic scale of both effects follows approximately a Gaussian distribution and the mean total signal is about 10^{-8} and 10^{-10} for the pqiCMB and pβ_t^2SZ effects, respectively. The polarization angle is consistent with a flat distribution in both cases. From the mean distributions of the polarization degree with redshift, the highest peak is found at $z \simeq 1$ for the induced CMB quadrupole and at $z \simeq 0.5$ for the kinematic component. Our results suggest that most of the contribution for the total polarization signal arises from $z \lesssim 4$ for the pqiCMB and $z \lesssim 3$ for pβ_t^2SZ. The spectral dependency of both integrated signals is strong, increasing with the frequency, especially in the case of the pβ_t^2SZ signal, which increases by a factor of 100 from 30 GHz to 675 GHz. The maxima values found at the highest frequency are about 3 μK and 13 μK for the pqiCMB and pβ_t^2SZ, respectively. The angular power spectra of these effects peak at large multipoles $\ell > 10^4$, being of the order of 10^{-5} μK^2 for pqiCMB polarization and 10^{-7} μK^2 for the pβ_t^2SZ effect. Therefore, these effects will not be a relevant source of contamination for measurements of the primary polarization modes, and at larger multipoles of roughly $\ell > 40{,}000$, pqiCMB may be the dominant component over the primary and lensing signals.

Key words: cosmic background radiation – galaxies: clusters: general – polarization – scattering

Online-only material: color figures

1. INTRODUCTION

Between the last scattering surface and the present time, photons are affected by perturbations, known as secondary anisotropies that will change the anisotropies pattern of the cosmic microwave background (CMB) radiation. At small angular scales, the interaction effects of the CMB photons when they pass through matter give information of the local large-scale structures (LSSs), matter distribution, and thermal history of the universe, allowing to establish constraints in the cosmological scenario.

At small angular scales, the dominant contribution for the secondary anisotropies caused by the scattering with the electrons along the line of sight (LOS) is known as the Sunyaev–Zel'dovich effect (SZE; Sunyaev & Zel'dovich 1970, 1972). This effect arises from the interaction of the CMB radiation with the electron gas in clusters of galaxies and filaments, due to its hot temperature or motion with respect to the CMB rest frame. This will be reflected in a tiny distortion of the intensity in the CMB spectrum. Due to the non-uniform CMB angular distribution, the scattering of the photons by this plasma will also change the intensity of the CMB radiation (Zel'dovich & Sunyaev 1980; Sunyaev & Zel'dovich 1981).

As happens with the intensity, it is expected that the CMB polarization also changes. During an emission or radiation transfer process, the polarization is caused by the presence of some type of asymmetry and the scattering by the particles along the LOS will affect the polarization of light (for more details about general polarization processes, see, e.g., Leroy 2000). As a consequence of Thomson scattering of the CMB photons by the electrons in the intracluster medium (ICM) and filaments, the CMB radiation will become polarized. The primary CMB quadrupolar component was measured by *COBE* (Smoot et al. 1992) and later by *WMAP* (Bennett et al. 2003). It is primarily the existence of this component that will cause a CMB quadrupole induced polarization signal in the direction of ionized gas clouds (Zel'dovich & Sunyaev 1980). The proper motion of this plasma with respect to the CMB will also result in an induced polarization signal (Sunyaev & Zel'dovich 1980).

Therefore, the study of the magnitude of these signals can give some clues about the evolution of the CMB quadrupole, which measured toward many galaxy clusters up to high redshift, could help to constrain the cosmic variance uncertainty (Kamionkowski & Loeb 1997; Portsmouth 2004; Bunn 2006) and probe three-dimensional information of potential fluctuations around our last scattering surface (Seto & Sasaki 2000). Furthermore, from the evolution of the integrated Sachs–Wolfe effect, the growth of CMB quadrupole can be used to trace the growth of the density fluctuations and prove the dark energy (Baumann & Cooray 2003; Cooray & Baumann 2003; Cooray et al. 2004). Moreover, measurements of the induced polarization can also give information about the dynamical state of the gas and on the peculiar velocity of clusters relative to the CMB

radiation (e.g., Sazonov & Sunyaev 1999; Lavaux et al. 2004; Shimon et al. 2006).

These quadrupolar and kinematic polarization effects in particular, come from a single scattering (single electron) events and will be the subject of study in this article. We do not considerer additional polarization effects arising from two consecutive scatterings (see, e.g., Sazonov & Sunyaev 1999; Lavaux et al. 2004; Shimon et al. 2006) and we neglect the presence in clusters of a central compact radio source (Sunyaev 1982; Holder & Loeb 2004), cold fronts (Diego et al. 2003), or the presence of other foregrounds, like point sources or dust. We also neglect relativistic corrections (Challinor et al. 2000; Itoh et al. 2000).

From previous studies about polarization effects in clusters of galaxies, very small induced polarization signals of the order of roughly 0.03 μK in the case of the quadrupole induced polarization are expected (Sazonov & Sunyaev 1999) and values higher than 1 μK have been pointed out for the kinematic component at large frequencies (Audit & Simmons 1999). However, with the advance in sensitivity and angular resolution of the recent and future space and ground-based sub/millimeter instruments at multi-frequency bands, as Planck, CMBPol, COrE, ACTpol, SPTpol, AMI, ALMA, among others, the detection and separation of the induced polarization by galaxy clusters and filaments at and below μK levels is becoming a reality. Therefore, is necessary to conduct a statistical study of the properties that characterize it, namely, the distribution of the polarization degree and angle and their time and frequency evolution.

With that aim, we produced sky patches realizations, each with an area of about 0.86 deg^2 at a resolution of $6''$, with redshifts roughly in the range 0.03 and 7.24, using N-body/hydrodynamic simulations. The adopted cosmological model is the standard ΛCDM model for a flat universe with *WMAP* cosmological parameters. The present-time cold dark matter, dark energy, and baryonic density parameters expressed in terms of the critical density are $(\Omega_{cdm}, \Omega_\Lambda, \Omega_b) = (0.256, 0.7, 0.044)$, respectively. It is assumed an equation of state for the dark energy component of $w = -1$, a present-day dimensionless Hubble constant of $h = 0.71$ and $T_0 = 2.725$ K for the mean CMB temperature. It is considered adiabatic ICs, a reionization fraction of 1 at redshift 7 and a scalar spectral index of $n_s = 1$. For the present epoch, it is assumed that the normalization of the fluctuations power spectrum is $\sigma_8 = 0.9$ with the linear power spectrum shape parameter of $\Gamma = 0.17$.

This article is structured as follows: In Section 2, the basic concepts and analytical formulae of the induced polarization by a single scattering are presented, followed in Section 3, by a description of the simulation method to produce the sky patches realizations. The results with the characterization of the polarization signals appear in Section 4, and the last section is dedicated to the conclusions and summary of the obtained results.

2. INDUCED POLARIZATION FROM SINGLE SCATTERING

The polarization of the CMB radiation is generated from Thomson scattering by free electrons of the photons of the incoming anisotropic radiation field.

The description of the local polarization state of an electromagnetic wave can be done through the Stokes parameters, namely, the scalars I, Q, U, and V. Consider the $\hat{z}$-axis as the wave propagation direction. The parameter I measures the total power in the wave and is proportional to the total intensity radiation (polarized and non-polarized), Q and U represent the linearly polarized component. We adopt here, by convection, $Q < 0$ ($Q > 0$) for a N–S (E–W) polarization component and $U > 0$ ($U < 0$) for a NE–SW (NW–SE) component. V describes the circular polarization, which in the case of Thomson scattering will not be created and with respect to the primary CMB anisotropies, at high frequencies (above ~30 GHz) or ignoring the presence of magnetic relativistic particles, can be neglected (e.g., Cooray et al. 2003).

The CMB polarization field can also be analyzed in a similar way as the temperature, however, besides the strength, the orientation needs to be considered. The Q and U are dependent of the coordinate system but the quantities I and $Q^2 + U^2$ are invariant under rotation of the $\hat{x}$–$\hat{y}$ plane. The degree of linear polarization is defined by

$$P = \sqrt{\left(\frac{Q}{I}\right)^2 + \left(\frac{U}{I}\right)^2} \tag{1}$$

and the angle of polarization with respect to the $\hat{x}$-axis, is given by

$$\phi = \frac{1}{2}\arctan\left(\frac{U}{Q}\right). \tag{2}$$

The differential Thomson scattering cross-section of an incident radiation field by an electron is given by

$$\frac{d\sigma_T}{d\Omega} = \frac{3\sigma_T}{8\pi}|\hat{\varepsilon}_{\rm in}\cdot\hat{\varepsilon}_{\rm out}|^2, \tag{3}$$

where $\hat{\varepsilon}_{\rm in}$ and $\hat{\varepsilon}_{\rm out}$ are the polarization unit vectors of the incoming (incident) and outgoing (after scattering) wave, respectively, σ_T is the Thomson cross-section and $d\Omega$ is the solid angle in the direction of incident radiation.

Integrating the incident radiation over all directions and considering the $\hat{z}$-axis as the propagation direction of the scattered radiation along the LOS, the Stokes parameters are given by (e.g., Kosowsky 1996; Seto & Sasaki 2000)

$$I(\hat{z}) = \frac{3\sigma_T}{16\pi}\int I^{\rm in}(\theta,\varphi)(1+\cos^2\theta)d\Omega \tag{4}$$

$$Q(\hat{z}) = \frac{3\sigma_T}{16\pi}\int I^{\rm in}(\theta,\varphi)\sin^2\theta\cos(2\varphi)d\Omega \tag{5}$$

$$U(\hat{z}) = -\frac{3\sigma_T}{16\pi}\int I^{\rm in}(\theta,\varphi)\sin^2\theta\sin(2\varphi)d\Omega. \tag{6}$$

Expanding the incident radiation in spherical harmonics,

$$I^{\rm in}(\theta,\varphi) = \sum_l\sum_m a_{lm}Y_{lm}(\theta,\varphi) \tag{7}$$

the linear polarization state can be compacted in the following expression:

$$Q(\hat{z}) - iU(\hat{z}) = \frac{3\sigma_T}{4\pi}\sqrt{\frac{2\pi}{15}}a_{22}, \tag{8}$$

where a_{22} represents the quadrupole component of the incident intensity field. This expression shows that an observer will detect polarization only if the quadrupole moment of the incident radiation is different from zero.

Under rotation by an angle α in a plane perpendicular to an arbitrary direction $\hat{n}$, the transformation of Q and U about the $\hat{z}$-axis can be condensed in the following expression (see, e.g., Zaldarriaga & Seljak 1997, and references therein):

$$(Q \pm iU)'(\hat{n}) = e^{\mp 2i\alpha}(Q \pm iU)(\hat{n}), \quad (9)$$

which makes of $(Q \pm iU)$ a spin ± 2 quantity that can be expanded in spin-s weighted spherical harmonics ${}_sY_{lm}(\hat{n})$ and reduced to a spin-0 quantity, like the scalar CMB temperature anisotropy, by using the so-called spin raising and lowering operators. In this way, that quantity can be expressed as

$$(Q \pm iU)(\hat{n}) = \sum_l \sum_m a_{\pm 2,lm}\ {}_{\pm 2}Y_{lm}(\hat{n}). \quad (10)$$

2.1. CMB Quadrupole Induced Polarization (pqiCMB)

Considering a single scattering, the dominant polarization effect induced in the direction of clusters of galaxies and filaments, arises from the presence of the intrinsic quadrupole component from the CMB temperature anisotropy. This effect will be denoted here by pqiCMB.

The pqiCMB is generated through the quadrupolar temperature fluctuation of the last scattering at clusters of galaxies and filaments locations (see, e.g., Seto & Sasaki 2000). In here, we consider the simplest and dominant source of the temperature perturbations, the scalar perturbation modes, which results from the gravitational instability by the density fluctuations. In scalar mode, the fluctuation produced by a single plane wave (Fourier mode) has axis symmetry, i.e., it is invariant under rotations around $\mathbf{k}$ (with $\mathbf{k}$ being the wavevector of a Fourier mode). Therefore, the temperature from a single plane wave can be written as (Ma & Bertschinger 1995)

$$\Delta_T(\mathbf{k}, \eta, \hat{\mathbf{n}}') = \sum_l (-i)^l \sqrt{4\pi(2l+1)}\Delta_{Tl}(\mathbf{k}, \eta)Y_{l0}(\hat{\mathbf{n}}'), \quad (11)$$

where the $\hat{\mathbf{n}}'$ indicates the direction of incident photon in the frame, where $\mathbf{k} \parallel \hat{\mathbf{z}}$ and η is the conformal time. Here, we have not summed up m due to the rotational symmetry of the scalar mode. Since the anisotropy at a given spacetime is superposed by plane-wave contributions, we need to use a general coordinate system in which $\hat{\mathbf{z}}$ is parallel to the LOS. To rotate the $\Delta_T(\mathbf{k}, \tau, \hat{\mathbf{n}}')$ in Equation (11) in the frame of $\mathbf{k} \parallel \hat{\mathbf{z}}$ to the general frame, we can use the generalized addition theorem

$$\sum_m Y^*_{lm}(\theta_1, \phi_1)Y_{lm}(\theta_2, \phi_2) = \sqrt{\frac{2l+1}{4\pi}}Y_{l0}(\beta) \quad (12)$$

with the β being the angle between (θ_1, ϕ_1) and (θ_2, ϕ_2). Putting the direction of $\mathbf{k}$ in (θ_1, ϕ_1) and direction of incident photon $\hat{\mathbf{n}}$ in (θ_2, ϕ_2), the Equation (11) can be rewritten as

$$\Delta_T(\mathbf{k}, \eta, \hat{\mathbf{n}}) = \sum_{lm} (-i)^l 4\pi \Delta_{Tl}(\mathbf{k}, \eta)Y^*_{lm}(\hat{\mathbf{k}})Y_{lm}(\hat{\mathbf{n}}), \quad (13)$$

where the $\hat{\mathbf{n}}$ indicates the direction of incident photon in the general frame.

From Equations (5), (6), and (13), we can calculate the Q_T and U_T in the real space by

$$dQ_T^{\Delta T_2} = \frac{3\sigma_T}{4}\int d^3\mathbf{k}e^{i\mathbf{k}\cdot\mathbf{x}}\Delta_{T2}(\mathbf{k}, \eta)\sin^2\theta_k\cos(2\varphi_k) \quad (14)$$

$$dU_T^{\Delta T_2} = -\frac{3\sigma_T}{4}\int d^3\mathbf{k}e^{i\mathbf{k}\cdot\mathbf{x}}\Delta_{T2}(\mathbf{k}, \eta)\sin^2\theta_k\sin(2\varphi_k) \quad (15)$$

with (θ_k, φ_k) being the direction of $\mathbf{k}$ in the general frame. Here, we have integrated over the direction of incident photon $\hat{\mathbf{n}}$ and used the orthonormal condition for spherical harmonics $\int Y^*_{lm}(\hat{\mathbf{n}})Y_{l'm'}(\hat{\mathbf{n}})d\Omega = \delta_{ll'}\delta_{mm'}$. Since $\sin^2\theta e^{2i\varphi} = \sqrt{32\pi/15}Y_{22}$, the orthonormal condition makes only $l = 2$ remain in Equations (14) and (15).

Hence, the integrated effect along the LOS is given by

$$Q_T = \frac{Q_v}{I_0 f(x)} = \int n_e dQ_T^{\Delta T_2} dZ, \quad (16)$$

$$U_T = \frac{U_v}{I_0 f(x)} = \int n_e dU_T^{\Delta T_2} dZ \quad (17)$$

where n_e is the electron density. Q_T and U_T denote here small changes in temperature $\Delta Q_T/T_0$ and $\Delta U_T/T_0$, respectively, corresponding to small changes in intensity $Q_v/I_0 = \Delta Q_v/I_0$ and $U_v/I_0 = \Delta U_v/I_0$.

The frequency dependence of the previous relations is given by I_0 and $f(x)$, which corresponds, respectively, to the intensity following the Planck's law of a blackbody spectrum with temperature T_0 and $f(x)$ is the usual conversion factor from temperature to specific intensity units,

$$f(x) = \frac{d\ln I(\nu)}{d\ln T} = \frac{xe^x}{e^x - 1}, \quad (18)$$

where x is defined as the dimensionless frequency parameter, $x \equiv h_P\nu/k_B\mathrm{T}$, with h_P and k_B being the Planck and the Boltzmann constants, respectively, and $I(\nu)$ is the Planck function for a given temperature.

2.2. Transverse Motion Induced Polarization ($p\beta_t^2SZ$)

Measurements of the CMB polarization from the single scattering by the electrons in the ICM moving with respect to the CMB can give information about the tangential velocity component of galaxy clusters in the LOS (Sunyaev & Zel'dovich 1980). This effect will be denoted here by $\mathrm{p}\beta_t^2\mathrm{SZ}$.

Considering the relative motion between a free electron and the CMB, from the relativistic Doppler effect and expanding in Legendre polynomials up to the second order,

$$T = \frac{T_0}{(1+\beta\mu)\gamma} \simeq T_0\left[1 + \beta\mu + \beta^2\left(\mu^2 - \frac{1}{3}\right) + \cdots\right], \quad (19)$$

where $\mu = \cos(\theta)$ with θ being the angle between the electron velocity v and the direction of the incident CMB photon, $\beta = v/c$ is the dimensionless velocity with c being the speed of light and $\gamma = (1-\beta^2)^{-1/2}$ is the Lorentz factor.

In the electron rest frame, the specific intensity is given by

$$I^{\mathrm{in}}(\nu) = 2\frac{h\nu^3}{c^2}\frac{1}{e^{x\psi} - 1} \quad (20)$$

with $\psi = (1+\beta\mu)\gamma$. Supposing the angular distribution of the radiation intensity has the form

$$I^{\mathrm{in}}(\nu) = I_0\left[1 + a\mu + b\left(\mu^2 - \frac{1}{3}\right) + \cdots\right], \quad (21)$$

where the coefficients a and b are frequency dependent. Then, the intensity of the radiation after scattering is given by

$$I^{\rm out}(\nu) = I^{\rm in}(\nu)(1-\tau_T) + I_0\tau_T\left[1 + 0.1b\left(\mu^2 - \frac{1}{3}\right)\right]. \quad (22)$$

The first term corresponds to the fraction of photons not scattered and the second term gives the scattered intensity. Hence, the induced polarization by the scattering will be proportional to the quadrupole term and b proportional to β^2 (see, e.g., Sunyaev & Zel'dovich 1981; Sazonov & Sunyaev 1999). The frequency dependence of the coefficient b can be found by expanding Equation (20) in Legendre polynomials, resulting in

$$b = f(x)h(x)\beta^2 \quad (23)$$

with $f(x)$ given by (18) and

$$h(x) = \frac{1}{2}x\frac{e^x+1}{e^x-1}. \quad (24)$$

In terms of Stokes parameters, the linear polarization is given by

$$Q_T = \frac{Q_v}{I_0 f(x)h(x)} = -0.1\int \sigma_T n_e \beta_t^2 \cos(2\chi)dZ \quad (25)$$

$$U_T = \frac{U_v}{I_0 f(x)h(x)} = -0.1\int \sigma_T n_e \beta_t^2 \sin(2\chi)dZ, \quad (26)$$

where $\beta_t^2 = \beta^2(1-\mu^2)$ is the dimensionless transverse velocity, which is perpendicular to the polarization plane and χ corresponds to the angle between this component and the $\hat{x}$-axis.

3. SIMULATION MODEL

In this section, we describe the simulation model used to produce Q_T and U_T fluctuations integrated along the LOS, through galaxy clusters and filamentary structures, in sky patches of about 1 deg^2, for both types of the aforementioned polarization effects. We start by describing the hydrodynamic N-body LSS simulations and the adopted map-making strategy. In the case of the pqiCMB polarization, this requires the construction of the primary CMB quadrupole along the CMB light path.

3.1. N-body/Hydrodynamic Simulations

The LSS simulations were produced with the public version of the code GADGET-2 (GAlaxies with Dark matter and Gas interacT), which includes smoothed particle hydrodynamics (SPH) to compute gas dynamics and an hierarchical Tree-PM algorithm to evaluate gravitational forces (Springel 2005). The cosmological integrations were made in comoving coordinates assuming periodic boundary conditions for boxes with a size of 100 h^{-1} Mpc on the side. The mesh size, used in the PM algorithm for the computation of the long-range gravity forces, was set to 512^3. We considered two types of particles in equal number, gas and dark matter (DM), with a total number of 2×276^3 particles. This corresponds to a mass resolution of about $3.38\times10^9\,h^{-1}\,M_\odot$ and $5.81\times10^8\,h^{-1}\,M_\odot$ for the DM and gas particles, respectively. In physical coordinates, the gravitational softening was held fix to $7.5\,h^{-1}$ kpc below $z=1$ and varied as $15/(1+z)\,h^{-1}$ kpc above this redshift.

The initial conditions (IC) snapshot was produced at redshift $1+z_{\rm i}=120$, with the COSMIC IC generator tool included in the public code package `hydra 4.2` (Couchman et al. 1995), and using the cosmological parameters described in Section 1. The simulation was evolved to redshift zero assuming adiabatic gas physics only. Simulation outputs were produced with the abutting boxes option switched on, which means that the redshift separation between consecutive outputs corresponds to the light travel time between boxes. In this way, boxes outputs stack smoothly along the LOS.

3.2. Primary CMB Quadrupole Polarization

In order to map the primary CMB quadrupole induced polarization, we need to compute the CMB quadrupole Stokes parameters, $dQ_T^{\Delta T_2}$ and $dU_T^{\Delta T_2}$, at the scattering points along LOSs. According to Equations (14) and (15), these can be computed directly from $\Delta_{T2}(\mathbf{k},\eta)$, provided the amplitude and evolution of each wavemode of Δ_{T2} is known. Since the evolution of $\Delta_{T2}(\mathbf{k},\eta)$ is independent of the direction $\mathbf{k}$, we may write

$$\Delta_{T2}(\mathbf{k},\eta) = \Delta_{T2}(k,\eta)\Psi_i(\mathbf{k}), \quad (27)$$

where $\Psi_i(\mathbf{k})$ is the initial perturbation and $\Delta_{T2}(k,\eta)$ is the solution of the Boltzmann equation with $\Psi_i = 1$. It is usual to assume that the two-point correlation function of the initial potential perturbations has the form

$$\langle\Psi_i^*(\mathbf{k})\Psi_i(\mathbf{k}')\rangle = P_\Psi(k)\delta^3(\mathbf{k}-\mathbf{k}'), \quad (28)$$

and the power spectrum $P_\Psi(k)$ obeys a power law

$$P_\Psi(k) = Ak^{n_s-4} \quad (29)$$

with A being a normalization factor and n_s being a spectral index of the scalar perturbations.

To compute the CMB quadrupole in a way that can be combined with the LSS simulation outputs, we generated (real space) volumes of the $dQ_T^{\Delta T_2}$ and $dU_T^{\Delta T_2}$ Stokes parameters, with the same size and at the same output times of the simulation snapshots. Inside each cubic volume, the conformal time is assumed constant, so that the time evolution of the quadrupole in each scattering point of the corresponding LSS simulation box matches the time of the scattering particle at that location (note that LSS simulation outputs are instant snapshots, i.e., inside a box all particles have the same cosmological time).

The computation of Equations (14) and (15) is then carried out in Fourier space, through the evaluation of Equation (27). The time evolution of the CMB quadrupole in each individual mode, $\Delta_{T2}(k,\eta)$, is computed using the CMBFast (Seljak & Zaldarriaga 1996) Boltzmann code, assuming the cosmological parameters adopted in this paper.

We show the results of numerically calculating the quadrupole power spectrum with CMBFast at the present day in Figure 1. Based on this result, we have uniformly sampled 400 modes in logarithm space from $k = 2\times10^{-5}$ to 10^{-2} h Mpc^{-1} in each dimension. We fixed this sampling and mode ranges for all conformal times required by the map-making strategy. The computation of $\Delta_{T2}(k,\eta)$ in the k-cubic grid is done using linear interpolation to estimate the amplitude of each mode from the CMBFast output at each conformal time.

The evaluation of $\Psi_i(\mathbf{k})$ is done for each wavemode by drawing a random number from a Gaussian distribution with variance given by Equation (28). We keep the same random

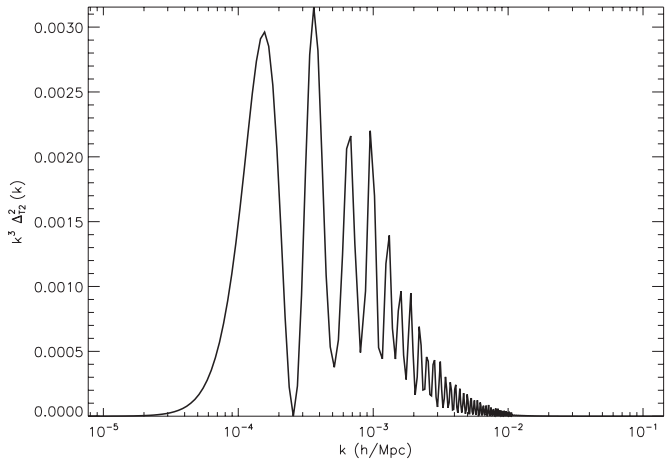

Figure 1. Power spectrum of the present-day quadrupole from the primordial CMB temperature anisotropies with arbitrary normalization. The power spectrum was calculated numerically with the CMBFast code.

realizations of $\Psi_i(\mathbf{k})$ at all conformal times, i.e., cubic volumes, of a stacking sequence. Different stacking sequences can be generated by changing the seed of our random number generator routine.

Having the information of the primordial CMB quadrupole in the k-space we perform the inverse Fourier transform in Equations (14) and (15) to obtain $dQ_T^{\Delta T_2}$ and $dU_T^{\Delta T_2}$ for all real space volumes of a given stacking sequence (i.e., sky map realization).

3.3. Map-making Method

In this work, we adopted the map-making strategy described in da Silva et al. (2000) and da Silva (2002). The method involves the stacking of LSS simulation boxes to generate random cosmological volumes, through which the relevant signals are integrated along a bundle of LOSs, i.e., a sky realization map. The randomization is obtained by preforming random symmetry operations (translation, rotations, and mirror reflections) on all particle positions of each LSS box of the stacking sequence. In this way, maps with the signal contribution from individual boxes are produced at each step (corresponding to a redshift interval) of the stacking sequence and then can be co-added to produce a total map that includes the integrated contribution from all redshifts. All these steps are included in the XSZMAP map-making code (da Silva 2002), which we use here to map the pqiCMB and pβ_t^2SZ polarization signals. This code has been intensively used in previous works (da Silva et al. 2000, 2001a, 2001b) to generate high-resolution SZE maps from N-body/hydrodynamic simulations.

The integration procedure in the XSZMAP code follows that in da Silva et al. (2000) and it is described in detail in da Silva (2002). According to the latter, the y Comptonization parameter of the thermal SZE (tSZE), defined as the integral along the LOS of the electron pressure

$$y = \frac{\sigma_T k_B}{m_e c^2} \int n_e T_e dl, \tag{30}$$

where m_e and T_e are the electron mass and temperature, can be computed in each pixel (LOS direction) as

$$y = \frac{\sigma_T k_B}{m_e c^2} \frac{m_{\rm gas}}{\mu_{\rm e} m_{\rm p}} \sum_{\rm i} T_{\rm i}\, I_{\rm W}(b_{\rm i}, h_{\rm i})\, /\mathcal{N}_{\rm i}. \tag{31}$$

The summation is carried out over any simulation particle, with temperature, T_i, gas mass, $m_{\rm gas}$, and SPH smoothing length $h_{\rm i}$, that is intercepted by the LOS direction with an impact parameter $b_{\rm i}$. The quantity $m_{\rm p}$ is the proton mass and $\mu_{\rm e} = 2/(X+1)$ is the mean molecular weight per free electron. Here, we assume a full ionized gas of hydrogen and helium with abundances $X = 0.76$ and $Y = 0.24$, respectively. The normalization factor

$$\mathcal{N}_{\rm i} = \Delta\Omega \sum_{b_{\rm i}} I_{\rm W}(b_{\rm i}, h_{\rm i}) \tag{32}$$

ensures that particle masses are conserved in the discretization process over pixels, each with angular area $\Delta\Omega$. For unresolved particles $\mathcal{N}_{\rm i} = \Delta\Omega$. Finally,

$$I_{\rm W}(b_{\rm i}, h_{\rm i}) = \int_{b_{\rm i}}^{2h_{\rm i}} W(z, h_{\rm i}) \frac{z}{\sqrt{z^2 - b_{\rm i}^2}}\, dz, \tag{33}$$

where $W(z, h_{\rm i})$ is the SPH smoothing kernel, given by the following S2 spline:

$$W(x, h_{\rm i}) = \frac{1}{4\pi h_{\rm i}^3} \begin{cases} 4 - 6x^2 + 3x^3, & 0 \leqslant x \leqslant 1 \\ (2-x)^3, & 1 < x \leqslant 2 \\ 0, & x > 2. \end{cases} \tag{34}$$

The map-making process is accelerated by pre-computing a table (with a thousand points) of the integral (33) as a function of impact parameters b, which is loaded into memory at the beginning of the code run. For a given, $b_{\rm i}$, the computation of $I_{\rm W}$ is then obtained through linear interpolation of the tabulated values.

The inclusion of the pβ_t^2SZ polarization in XSZMAP code is straightforward, given that the N-body simulations provide a simple way of computing β_t^2 and χ in Equations (25) and (26) for each particle. We have

$$Q_T^{\beta_t^2 SZ} = -0.1\, \sigma_{\rm T} \frac{m_{\rm gas}}{\mu_{\rm e} m_{\rm p}} \sum_{\rm i} \beta_{t,{\rm i}}^2 \cos(2\chi_{\rm i})\, I_{\rm W}(b_{\rm i}, h_{\rm i})\, /\mathcal{N}_{\rm i}, \tag{35}$$

$$U_T^{\beta_t^2 SZ} = -0.1\, \sigma_{\rm T} \frac{m_{\rm gas}}{\mu_{\rm e} m_{\rm p}} \sum_{\rm i} \beta_{t,{\rm i}}^2 \sin(2\chi_{\rm i})\, I_{\rm W}(b_{\rm i}, h_{\rm i})\, /\mathcal{N}_{\rm i}. \tag{36}$$

Here, we use the upper index "$\beta_t^2 SZ$" to denote the integrated Q_T and U_T Stokes parameters for the pβ_t^2SZ polarization.

To map the pqiCMB polarization parameters, we require additional information about the CMB quadrupole along the LOS. Our approach, which is detailed in Section 3.2, consists of generating the CMB quadrupole in cubic volumes of the same size and at the same redshifts of the hydrodynamic N-body simulation boxes containing the LSS particle information. For each sky realization, the CMB quadrupole is computed separately and stored in files that are read by the XSZMAP code to generate the maps. In this way, the integrated Stokes parameters for the pqiCMB polarization, here denoted with the upper index "qiCMB," can be computed in the following way:

$$Q_T^{\rm qiCMB} = \frac{m_{\rm gas}}{\mu_{\rm e} m_{\rm p}} \sum_{\rm i} dQ_{T,{\rm i}}^{\Delta T_2}\, I_{\rm W}(b_{\rm i}, h_{\rm i})\, /\mathcal{N}_{\rm i}, \tag{37}$$

$$U_T^{\rm qiCMB} = \frac{m_{\rm gas}}{\mu_{\rm e} m_{\rm p}} \sum_{\rm i} dU_{T,{\rm i}}^{\Delta T_2}\, I_{\rm W}(b_{\rm i}, h_{\rm i})\, /\mathcal{N}_{\rm i}, \tag{38}$$

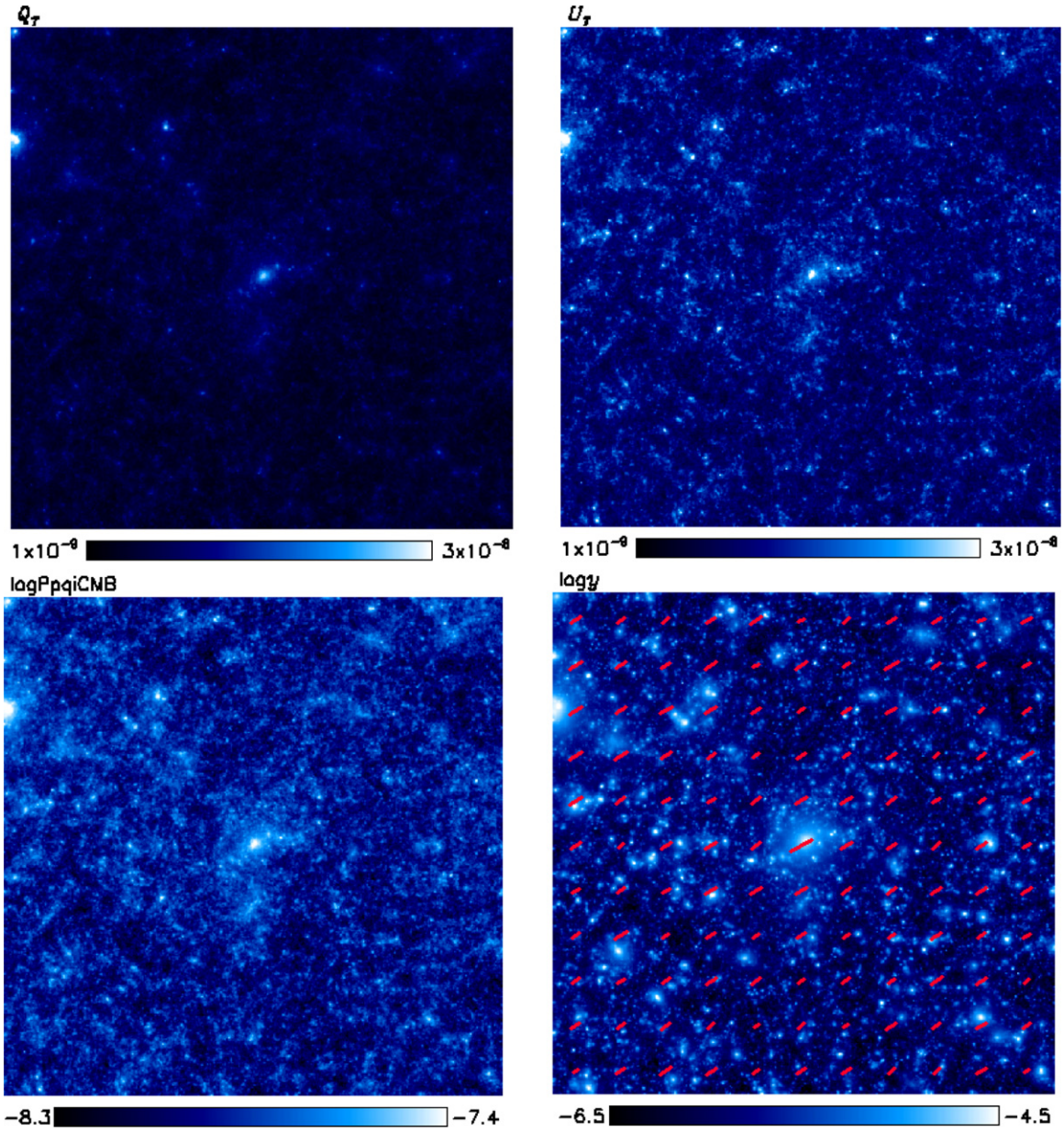

Figure 2. From the left to the right, Q_T, U_T (top) and log P, log y (bottom) maps of $0.^{\circ}93 \times 0.^{\circ}93$ integrated in redshift of one sky patch realization, for the pqiCMB effect. The (red) vectors on the log y maps represent the magnitude of the polarization degree and the orientation is given by the polarization angle. The maps are color scaled for better visualization.

where the $dQ_{T,\mathrm{i}}^{\Delta T_2}$ and $dU_{T,\mathrm{i}}^{\Delta T_2}$ are the CMB quadrupole components at the particle locations, given by Equations (14) and (15), respectively. These are obtained using trilinear interpolation from the pre-computed CMB quadrupole cubes.

In total, we generated 28 random sky patch realizations for all the above effects, each with an area of about 0.86 deg^2 and a pixel resolution of $6''$ on the side. Our highest redshift of integration is $z = 7.24$, beyond which we assume gas is no longer ionized.

4. RESULTS

4.1. Characterization of the Total Signal

4.1.1. Simulated Sky Patches

We present in Figures 2 and 3 a typical sky realization of the pqiCMB and pβt^{2}SZ effects, respectively, integrated along a light cone. In both the figures, the two top panels show total maps of the frequency-independent polarization parameters, Q_T and U_T, and the two bottom panels shows the tSZE (Compton y-parameter) and the polarization degree maps (both in logarithm scale) arising from the same sky region. Overplotted on the log y maps are (red) vectors representing the magnitudes of the polarization degree, P, obtained from Equation (1), with the orientation given by the polarization angle, ϕ, calculated with Equation (2).

From Figure 2, we can see in the log y map that the pqiCMB polarization vectors align almost uniformly in the small sky patch, a phenomenon that also appears in the other 27 sky patch realizations (although with different global directions due to the random realizations). This confirms expectations, because the primary CMB temperature quadrupole has variations on much larger angular scales than those probed by our maps (see, e.g., Cooray & Baumann 2003; Baumann & Cooray 2003, and

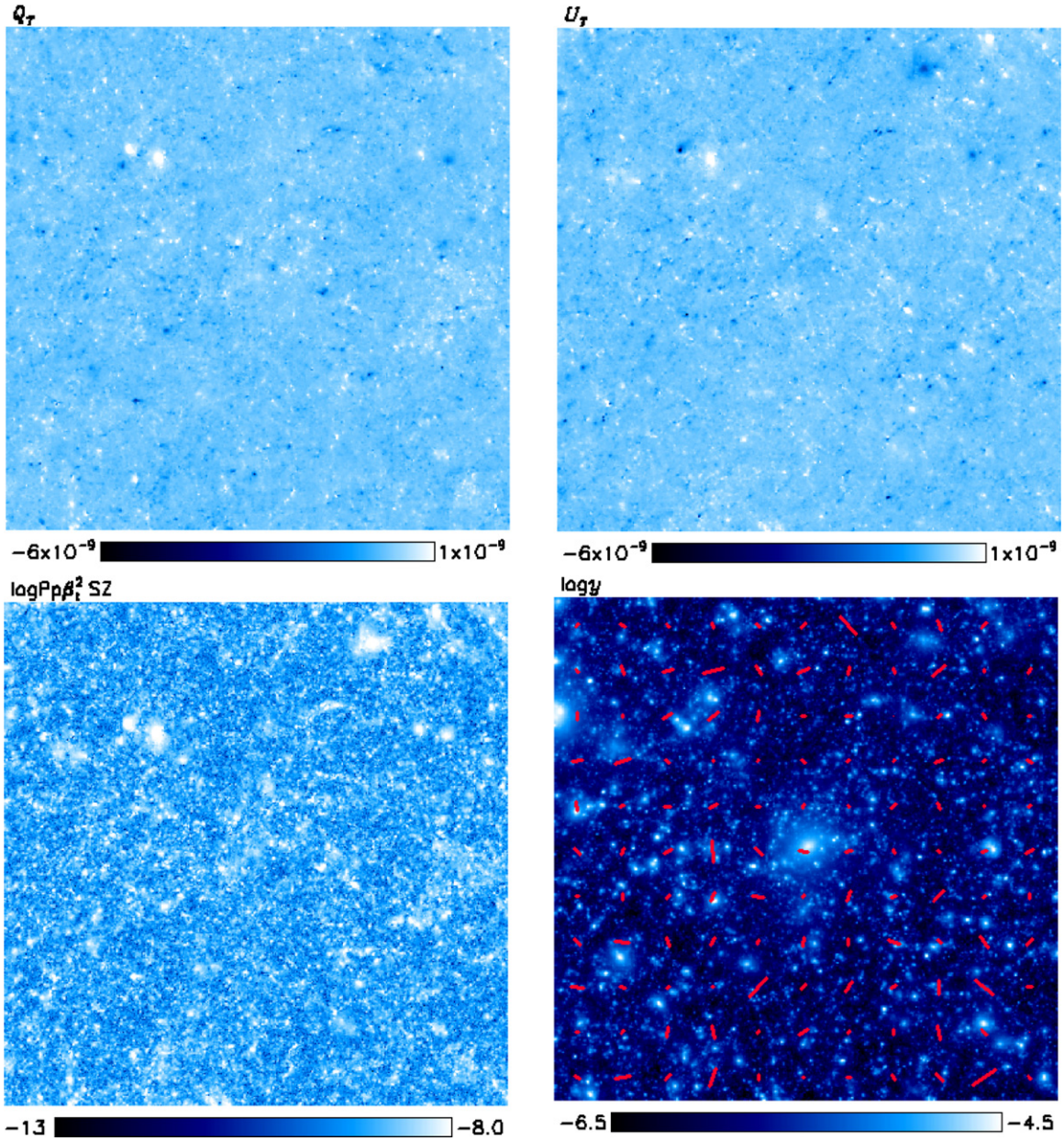

Figure 3. Same as Figure 2, but for the pβ_t^2SZ effect.

references therein). Therefore, in small sky patches of degree order and integrated over depths smaller than the variation length of the primary CMB temperature quadrupole, the variance of the magnitude of the induced polarization pqiCMB is mainly determined by the variance of the optical depth, $\tau = \int \sigma_T n_e dl$. Since our integration range goes from $z \sim 0$ up to $z \sim 7$, the primary CMB temperature quadrupole is expected to vary within this range of redshifts and therefore our total pqiCMB signal should be visually similar to an optical depth map weighted by the variation of the primary CMB temperature quadrupole along the LOS. We confirmed this by simulating integrated (total) optical depth maps of our sky realizations, which look similar (but not identical) to the linear polarization degree, log P pqiCMB, maps. In Figure 2, we also see that many structures that are visible in the log y map are also visible in the log PpqiCMB map. However, one should note that since the tSZE signal is also weighted by temperature, bound structures like galaxy clusters are enhanced with respect to the mean background.

Contrary to the pqiCMB polarization, the pβt^{2}SZ polarization angles are not uniform in the maps, as it can be observed from the orientation of the (red) vectors on the bottom right panel of Figure 3. Also the magnitudes can add to zero resulting in null polarization vectors at some locations. These effects are a consequence of the transverse velocity distribution of the scattering gas and of the integration along the LOS that tend to erase contributions from individual sources. Because of this, it is a lot less obvious to try to find a visual correspondence between the pattern of structures in the log Ppβ_t^2SZ and log y maps.

4.1.2. Pixel Distributions

Collecting all pixel values in the 28 sky realizations, we computed sky-averaged pixel distributions of $log P$ and ϕ.

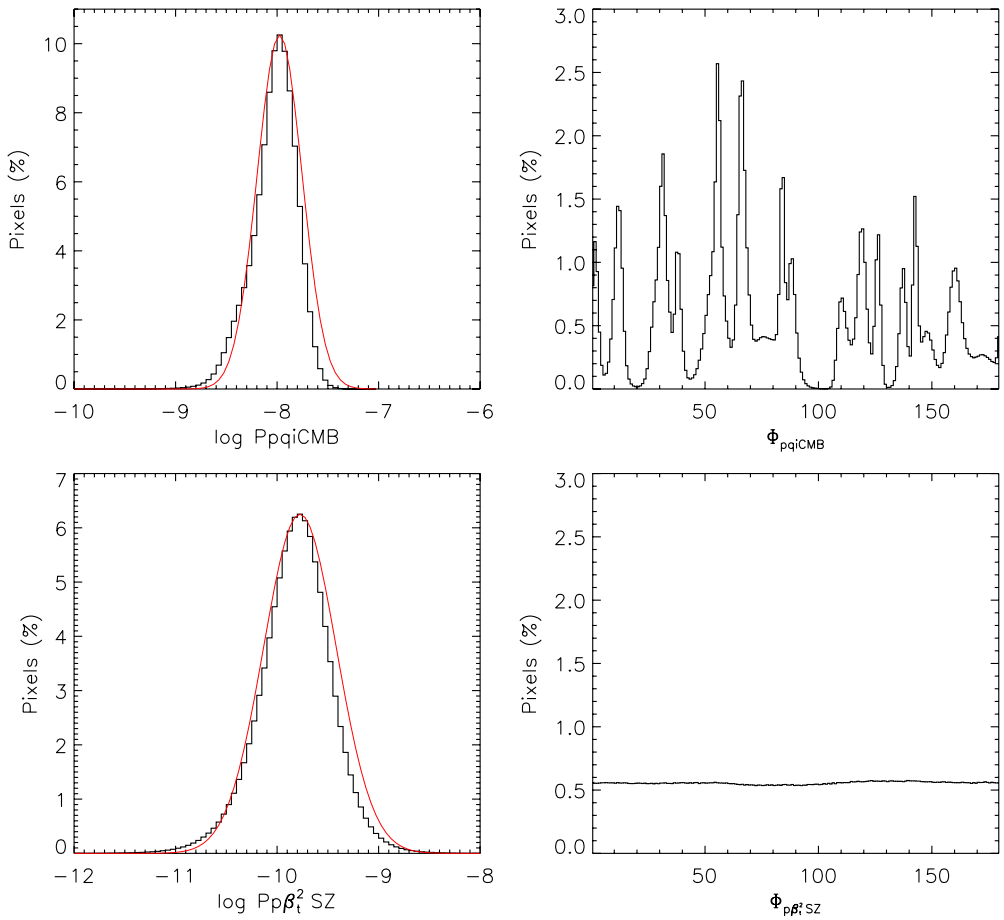

Figure 4. Histograms normalized in percentage of the polarization degree in logarithm scale (left) and polarization angle (right) for the pqiCMB (top) and pβ_t^2SZ (bottom) effects. The (red) solid lines correspond to Gaussian distributions with the standard deviations σ given in Table 1.

(A color version of this figure is available in the online journal.)

Table 1
Moments

Property	Mean	Median	σ	Min	Max	Skewness	Kurtosis
log(PpqiCMB)	−8.0	−8.0	0.2	−11.2	−7.0	−0.7	1.1
$\phi_{\rm pqiCMB}$	82	70	49	0	180	...	...
log(Ppβ_t^2SZ)	−9.8	−9.8	0.4	−13.1	−7.2	−0.3	1.2
$\phi_{\rm p\beta_t^2SZ}$	90	91	52	0	180	...	...

Results are display in Figure 4 for the pqiCMB (top panels) and pβt^{2}SZ (bottom panels) polarizations. All curves are normalized to the total number of pixels in the 28 sky realization maps. The corresponding statistical moments, maximum and minimum values of the polarization signals are also presented in Table 1. In the log P plots of Figure 4 we also show Gaussian curves (red solid lines) centered at the mean values, with standard deviations presented in Table 1. The amplitudes of these curves were set to match the maximum values of the pqiCMB and pβt^{2}SZ histograms.

These results clearly indicate that the pqiCMB signal dominates over the pβt^{2}SZ polarization signal. Although the tails of both pixel distributions can reach values of about 10^{-7}, we clearly see that the bulk of the pixels in the pqiCMB maps have polarizations larger than 10^{-9}, whereas the majority of pixels in the pβt^{2}SZ maps have linear polarization degrees smaller than this value. The mean value of P for the pqiCMB polarization is about 10^{-8}, which is consistent with previous results (Sazonov & Sunyaev 1999; Cooray & Baumann 2003; Amblard & White 2005). This is about two orders of magnitude larger than the mean pβt^{2}SZ polarization, 2×10^{-10}, obtained in our simulations.

The polarization degree distributions are peaked around the mean values and show approximate lognormal shapes with tails that are less symmetric (two times more negatively skewed) in the case of the pqiCMB polarization. This is due to the different nature of the effects. In the case of the pqiCMB polarization, the left tail of the distribution arises mostly due to low-density diffuse gas, whereas the high-end tail is due to dense gas in halos and galaxy clusters. In the case of the pβt^{2}SZ polarization, gas from dense regions may contribute to any signal in the distribution, depending on its transverse (sky projected) velocities.

The histograms in the right panels of Figure 4 show different shapes for the distributions of polarization angles of pqiCMB and pβt^{2}SZ, however, they are both consistent with a flat distribution (see also Table 1). The peaks in the $\phi_{\rm pqiCMB}$ plot are due to the distribution of polarization angles from individual sky realization maps. As noted in the previous section, the pqiCMB maps from a single sky realization show little variation of polarization angles due to the small angular area of our maps (see Figure 2). Therefore each sky realization contributes with a strongly peaked distribution of angles, centered at the mean polarization angle in each map, to the total distribution of angles in Figure 4. Since the generation of sky realizations

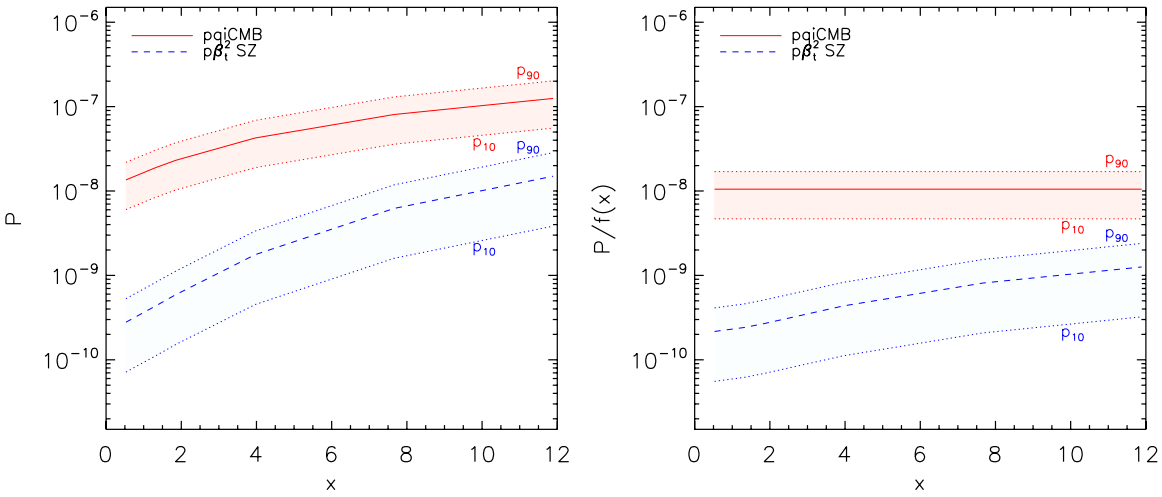

Figure 5. Polarization degree as a function of frequency with x the dimensionless frequency and $f(x)$ given by Equation (18). The $\hat{y}$-axis is logarithmic scaled. The (red) solid and (blue) dashed lines correspond to the mean over all simulations for the pqiCMB and pβ_t^2SZ, respectively. The dotted lines represent the 10th percentile (p_{10}) and 90th percentile (p_{90}) for each polarization effect.

(A color version of this figure is available in the online journal.)

Table 2
Frequency Dependency

Frequency		pqiCMB			pβ_t^2SZ		
(GHz)	x	$\langle \log P \rangle$	Min($\log P$)	Max($\log P$)	$\langle \log P \rangle$	Min($\log P$)	Max($\log P$)
30	0.53	−7.9	−11.1	−6.9	−9.7	−13.0	−7.1
75	1.32	−7.8	−10.9	−6.8	−9.5	−12.8	−6.9
105	1.85	−7.7	−10.8	−6.7	−9.4	−12.6	−6.7
225	3.96	−7.4	−10.6	−6.4	−8.9	−12.2	−6.3
435	7.66	−7.1	−10.3	−6.1	−8.4	−11.6	−5.7
675	11.9	−7.0	−10.1	−6.0	−8.0	−11.2	−5.3

is random, the resulting polarization angle distribution of the 28 sky realizations generated for this paper displays a high number of peaks and valleys corresponding to the overposition of individual map realizations. We verified that increasing the number of random realizations tends to produce a uniform distribution of $\phi_{\rm pqiCMB}$.

4.1.3. Frequency Dependence of the Polarized Signals

True sky polarizations are frequency-dependent quantities and the spectral dependence of the pqiCMB and pβ_t^2SZ polarization degrees are given by $f(x)$ and $f(x)\,h(x)$, respectively, with $f(x)$ given by Equation (18) and $h(x)$ by Equation (24). To better infer the magnitudes of the frequency-dependent polarizations we list in Table 2 the maximum, minimum, and mean polarization degrees in our pqiCMB and pβ_t^2SZ maps at six frequencies, namely, 30, 75, 105, 225, 435, and 675 GHz. These correspond to typical frequencies of the next generation sub/millimeter telescopes, such as the ALMA interferometer and the space mission proposal *COrE*.

We start by looking at the magnitudes of maximum polarization degrees in our maps, as these are the signals with highest chance of being detected by polarization experiments. From Table 2 we see that maximum pqiCMB polarization raises from 0.3 μK at 30 GHz up to 3 μK at 675 GHz. These amplitudes are found in the direction of the brightest polarization source, a galaxy cluster, appearing in our 28 sky realization maps. For the pβ_t^2SZ polarization, the highest polarization degree in our maps ranges from 0.2 μK at 30 GHz up to 13 μK at 675 GHz. For both cases, the maximum degree of polarization increases with frequency. We note, however, that these maxima can be obtained at different locations of the pqiCMB and pβ_t^2SZ maps and therefore a comparison between the maxima of both types of polarization needs to be carefully done.

A better way of comparing the frequency dependence of the pqiCMB and pβ_t^2SZ polarization degrees is to look at the mean degree of polarization in the 28 sky realization maps. These are shown in the left panel of Figure 5. The (red) solid and (blue) dashed lines are the mean pqiCMB and pβ_t^2SZ polarization degrees, respectively, averaged over the 28 sky realizations. The dotted lines are the 10th and 90th percentiles considering all values of the 28 realizations at each frequency. It is clear from this figure and Table 2, the strong frequency dependence of the mean polarization degree of both polarization effects, especially in the case of pβ_t^2SZ, which increases roughly by a factor of 100 from 30 GHz to 675 GHz. In the Rayleigh–Jeans (longwave) spectral region, this dependency vanishes but becomes significant in the Wien (shortwave) region (e.g., Sazonov & Sunyaev 1999; Audit & Simmons 1999). At high frequencies, the mean value of P at 675 GHz increases to about 10^{-7} and 10^{-8} for pqiCMB and pβ_t^2SZ, respectively. However, the mean pβ_t^2SZ polarization is always subdominant with respect to the pqiCMB mean signal in the range of the displayed frequencies. The maximum value found for the kinematic component at high frequencies in our simulations is consistent with previous results of Audit & Simmons (1999) and Shimon et al. (2006).

The right panel of Figure 5 shows the characteristic spectral signature of the pβ_t^2SZ polarization, which is of ultimate

importance for the detection and separation of this type of polarization from other components (Cooray & Baumann 2003), and the frequency independence of pqiCMB when expressed in temperature units. It is also clear that the relative strength of pqiCMB with respect to pβ_t^2SZ becomes more relevant in the Rayleigh–Jeans region.

4.2. Signal Dependence with Redshift

Our simulations allow us to address the issue of how the pqiCMB and pβ_t^2SZ polarization signals are distributed along the light cones of our 28 sky realization maps. This study can be carried out by examining the signal from individual boxes of the stacking sequence contributing to the sky realization maps. In total, 61 contiguous boxes, ranging from $z \simeq 0.034$ to $z \simeq 7.24$ and each with a comoving depth of $100\,h^{-1}$ Mpc (box size), are used to produce a total map.

Figure 6 shows the polarization degree, $\log P$, and angle ϕ of six boxes, at redshifts 0.03, 0.5, 1, 2, 3, and 7, contributing to the staking sequence of the same sky realization presented in Figures 2 and 3. The top panels of Figure 6 show the pqiCMB polarization signal whereas the bottom panels show the pβ_t^2SZ polarization patterns, arising from the boxes at these redshifts. In the figure, the amplitude of the polarization degree is color coded within the same ranges at all redshifts for each polarization effect and the polarization directions were set with the same size in all panels.

It can be seen from these maps that both effects follow the local distribution of gas. In the case of the pqiCMB effect, because the CMB quadrupole is practically constant within the box volume contributing to each map, the polarization pattern of $\log P$ closely follows the distribution of the gas column densities and the polarization angles are closely aligned in each panel. The variation of ϕ is also slow from panel to panel, i.e., along z, but it can be larger than the variation within each map (see, e.g., the polarization directions in maps at $z = 0.03$ and $z = 7$). In the case of the pβ_t^2SZ maps, the column densities are weighted by the square of the transverse velocity of the gas at each scattering location inside the column. This causes a large range of polarization orientations and structures with polarization amplitudes enhanced or dimmed depending on their internal velocity structure. For example, the brightest pqiCMB polarization source in the $z = 0.03$ map, which is the highest optical depth source within the box volume contributing to this map, is strongly dimmed in the pβ_t^2SZ map. A case where individual sources appear enhanced due to their velocity structure is, for example, the group of objects in the lower left corner of the maps at $z = 1$.

We note that the integration of signal from the observer up to high redshift can significantly degrade the imprint of individual structures we see in these maps due to the overlap of signal along the LOS. This effect, which is fully integrated in our simulations and lacking in other studies focusing on the polarization from individual objects, is particularly important in the case of the pβ_t^2SZ polarization, where the contribution from individual objects can be suppressed due to gas mixing.

To assess the redshift distribution of the signal in our maps, we computed the mean polarization degree per redshift interval, $d\langle P\rangle/dz$, and the respective cumulative distribution, $\langle P\rangle(< z)$, as a function of z. The results are displayed in the top and bottom panels of Figure 7 for the pqiCMB and pβ_t^2SZ polarization, respectively. The solid (red) lines are averages over the 28 sky realizations and the dotted lines are obtained from the individual maps at each redshift corresponding to the 10th and 90th percentiles. The shaded regions (including the dotted lines) enclose the results from 23 sky maps. The $d\langle P\rangle/dz$ curves are wiggly and the map-to-map dispersions are larger at lower redshifts due to the fixed angular size of the maps, which implies signal integrations over smaller physical volumes at lower z. This results from having by chance, a large or small number of polarization sources inside the probed volume.

Our results show that the redshift distribution of the pqiCMB polarization is highest at around $z \simeq 1$ and the total signal is mostly contributed below $z \lesssim 4$. According to the top right panel in Figure 7 about 93% of the signal arises from below this redshift. At higher z, the pqiCMB polarization decreases significantly and become practically converged by $z = 7.24$. In the case of the pβ_t^2SZ polarization, signal convergence is obtained at lower z, with most of the signal, about 93%, being generated below $z \lesssim 3$. The peak of the $d\langle P\rangle/dz$ curve also occurs at lower redshifts, $z \simeq 0.5$, when compared with pqiCMB polarization curve. The level of dispersion in pqiCMB plot is larger than the observed in the pβ_t^2SZ plot, which is a result of the large CMB quadrupole map-to-map variances inside the small angular area probed by our simulations.

4.3. Angular Power Spectra

We now turn to the characterization of the angular power spectra of the pqiCMB and pβ_t^2SZ polarization maps. Since the Q and U Stokes parameters depend on the coordinate system we computed the angular power spectra after transforming our maps into reference-frame independent quantities, the scalar E, and pseudo-scalar B-mode polarizations, for both effects. The details of the transformation and our power spectrum computation procedure are described in the Appendix.

In Figure 8, we present the angular power spectra of the pqiCMB (solid red line) and pβt^{2}SZ (dashed blue line) frequency-independent polarizations. We verified that in the case of these induced effects, the E- and B-mode power spectra have the same amplitudes, and therefore the solid and dashed lines represent both modes for each type of polarization. In the figure is also overplotted the primary CMB E-mode polarization (dotted purple line) and the B-mode polarization arising from the conversion of the primary CMB E-modes by gravitational lensing (triple dot-dashed green line). Both of these spectra were obtained using the public code CAMB (Lewis et al. 2000).

Our results indicate that pqiCMB and pβt^{2}SZ signals have similar shapes and show a gradual increase of amplitudes up to maxima of $\sim 10^{-5}$ μK^2 and $\sim 10^{-7}$ μK^2, respectively, at $\ell \sim 25{,}000$. It can also be seen from this figure that the power of pβt^{2}SZ is about 100 times smaller than the pqiCMB signal in the displayed range of multipoles. The results also confirm that the pqiCMB and pβt^{2}SZ polarizations from clusters and filamentary structures are clearly subdominant with respect to the primary CMB E-mode and lensing B-mode polarizations in a wide range of multipoles. These results are consistent with those of Baumann et al. (2003), Amblard & White (2005), and Shimon et al. (2009), and differ from those in Liu et al. (2005), who used a semianalytical method to compute the pqiCMB power spectra.

We also note that for our assumed cosmology, the primary CMB E-mode polarization dominates over the other effects up to $\ell \sim 6000$. At this multipole, the pqiCMB power is about 3 orders of magnitude smaller than the primary CMB. At lower multipoles, the difference is even larger. At higher multipoles, the CMB lensing B-mode polarization is a significant component of the polarization signal. For example, at $\ell = 8000$ the pqiCMB

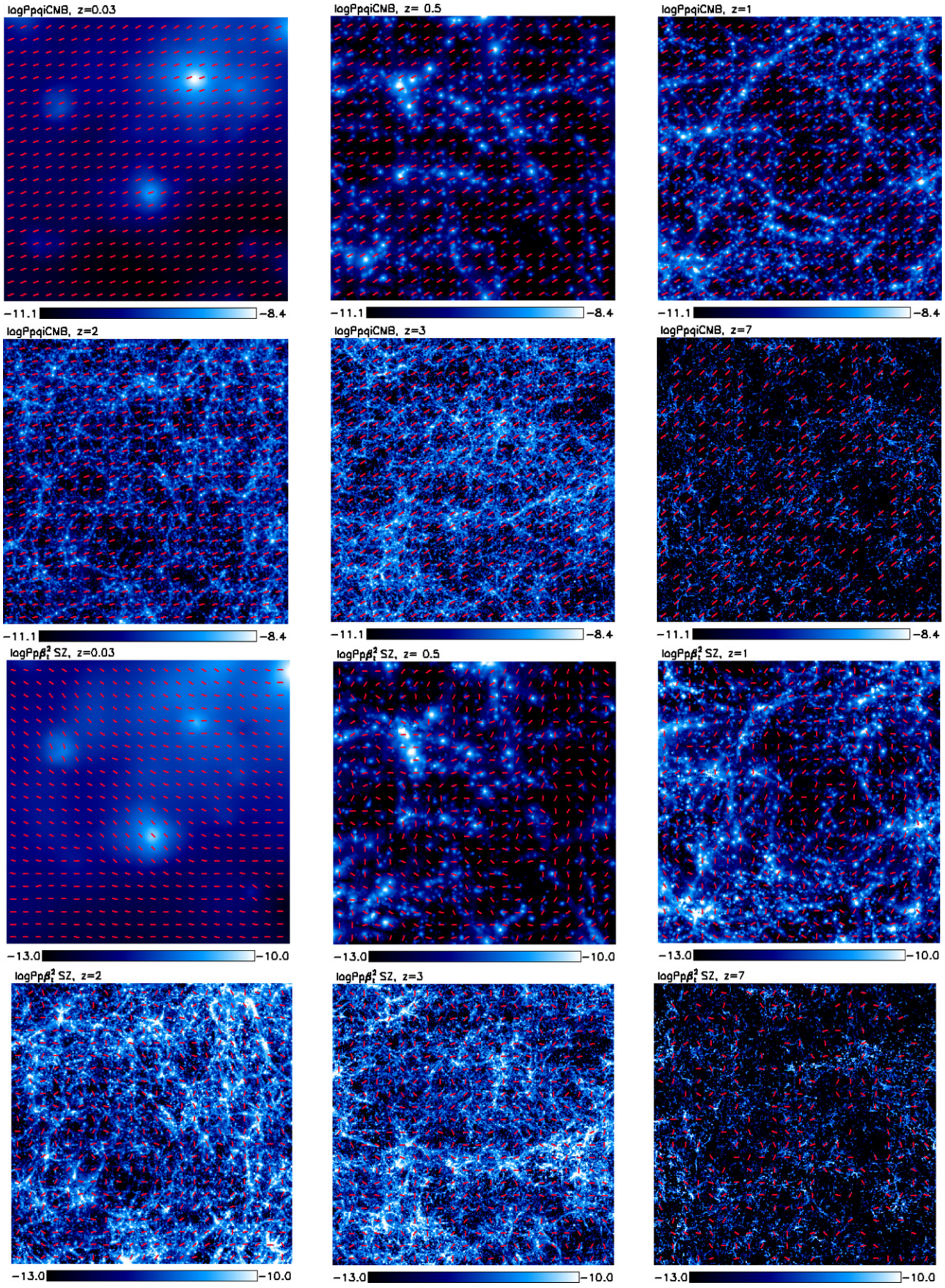

Figure 6. Polarization degree maps of $0.^{\circ}93 \times 0.^{\circ}93$ in logarithm scale, from the left to the right, for the redshifts 0.03, 0.5, 1, 2, 3, and 7, of one sky patch realization. The six panels on the top (bottom) corresponds to pqiCMB ($p\beta_t^2$SZ). The (red) vectors on the maps represent the polarization angles. The maps are color scaled for better visualization.

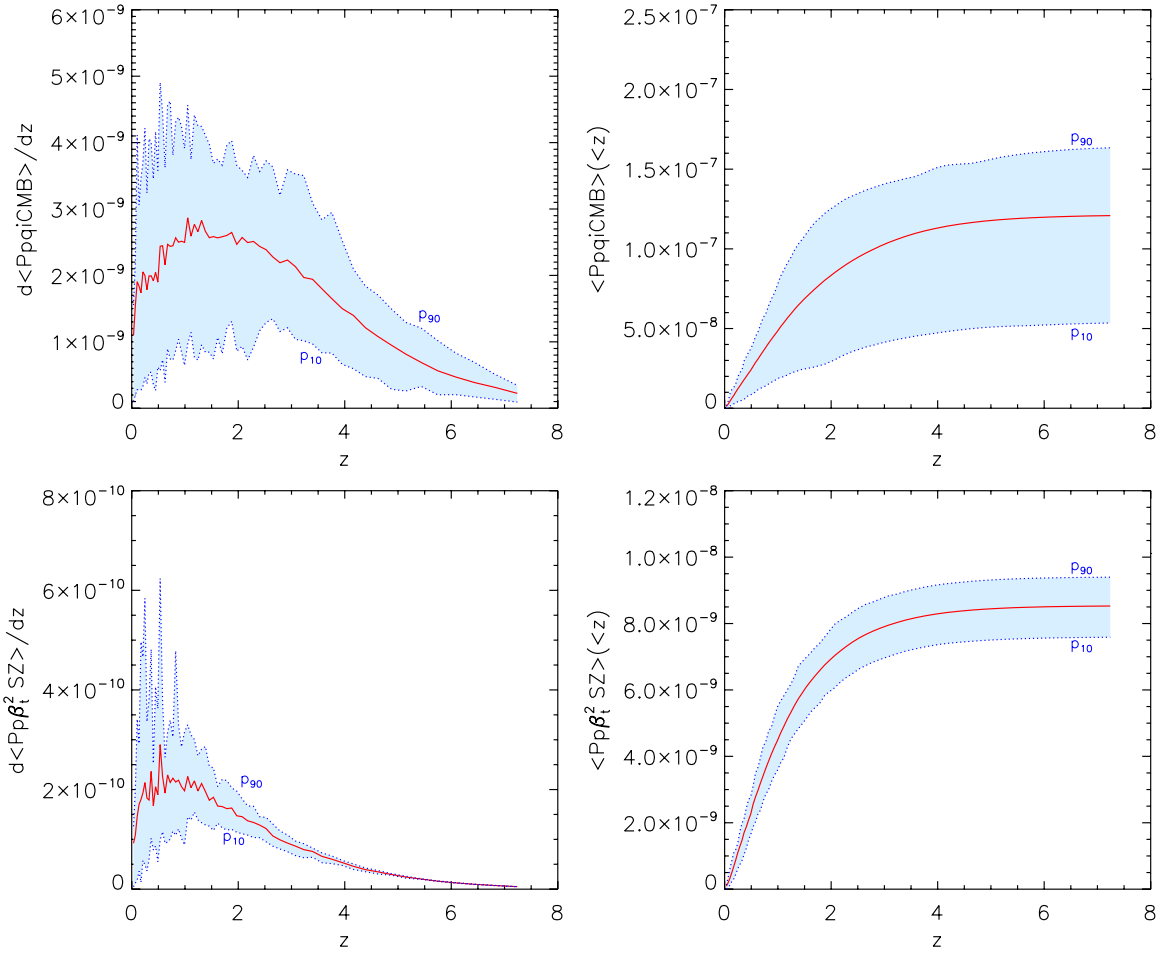

Figure 7. Differential polarization degree as a function of redshift (left) and respective cumulative distribution (right) for the pqiCMB (top) and pβ_t^2SZ (bottom) effects. The (red) solid line corresponds to the mean over all simulations and the (blue) dotted lines to the 10th percentile (p_{10}) and 90th percentile (p_{90}).

(A color version of this figure is available in the online journal.)

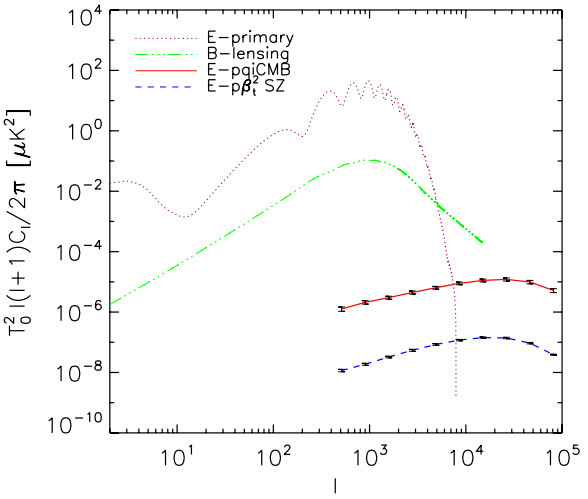

Figure 8. Polarization power spectra of pqiCMB (solid red line) and pβ_t^2SZ (dashed blue line) effects. The *B*-modes were omitted since they follow the same curve of *E*-modes. The error bars are statistical errors at 1σ confident level obtained by bootstrap resampling the set of maps. It is also shown the power spectra of the *E*-modes for the CMB primary (dotted purple line) and the lensing *B*-modes (triple dot-dashed green line), both obtained with the CAMB code.

(A color version of this figure is available in the online journal.)

spectra is more than 2 orders of magnitude smaller than the *B*-lensing polarization power. This difference gets reduced to about one order of magnitude at $\ell = 16{,}000$ and tends to decrease progressively with ℓ. At very large multipoles of about $\ell \sim 40{,}000$, the pqiCMB may dominate over the other three effects.

Considering the spectral dependency, the power increases with frequency but pqiCMB still dominates over pβt^{2}SZ (Shimon et al. 2009).

5. CONCLUSIONS

The study of polarization that arises between the last scattering surface and the present time, from the scattering of the CMB photons in the electron gas of clusters of galaxies and filaments, can give some clues about the global distribution of matter, reionization epoch of the universe and locally, and information about the dynamical state of galaxy clusters and primary CMB quadrupole. The exploitation of this type of information ultimately depends on the angular scale and relative amplitude of the polarization effects.

We analyze the properties of the two induced polarization effects arising from the single scattering of the CMB photons by the ionized gas, the origin of which is the presence of the CMB quadrupolar component (pqiCMB) and the gas motion transverse to the LOS (pβ_t^2SZ).

Instead of using an analytical model mostly adopted in previous studies or simulations of individual galaxy clusters, we used high-resolution *N*-body/hydrodynamic simulations featuring adiabatic gas physics and a novel box-stacking scheme that allows to reconstruct the CMB quadruple component and the physical properties of the scattering media along the light cone traversed by radiation. The maps obtained in this way, which fully contain the LOS contribution from collapsed structures, diffuse gas in filaments and low-density regions, allows us to address important issues about detection of secondary polarization and selection effects of polarization observations. We focus our study on the characterization of the induced polarized signals from their statistical properties in simulations at high angular resolution.

Our simulations confirm that the polarization degree of the pqiCMB is a close proxy of the electron density column and the polarization angles of this effect are closely aligned due to the slow variation of primary CMB quadrupole on small sky patches along the LOS. The effect of the gas overlap along density columns causes galaxy clusters and other bound objects to be less prominent (with respect to the mean background) than in the case of the thermal SZ effect, where the signal in clusters is boosted by the high temperature. In the case of pβ_t^2SZ, the polarization degrees and angles are weighted by the transverse velocity of the scattering media, therefore the integration along the LOS can erase contributions from individual collapsed objects, depending on their internal velocity structure and the effect of gas overlap.

The results from the pixel distribution in the frequency-independent maps show that the linear polarization degrees follows, in logarithm scale, nearly Gaussian distributions, centered around 10^{-8} and 10^{-10} for pqiCMB and pβ_t^2SZ, respectively, and both signals can reach maximum values of about 10^{-7}. The lognormal shape is a less good approximation in the case of the pqiCMB polarization, which reveals a relatively larger negative skewness. The distribution of polarization angles in both effects is consistent with being uniform if a sufficiently large number of sky patches is analyzed for the pqiCMB polarization.

By producing maps of these secondary induced polarization effects at six different frequencies, namely, 30, 75, 105, 225, 435, and 675 GHz, we confirm the strong dependence on frequency of both signals, especially in the case of pβ_t^2SZ, for which the mean value increases approximately by a factor of 100 from the 30 GHz to 675 GHz. In temperature units, the maxima signals increase from around 0.3 μK (pqiCMB) and 0.2 μK (pβ_t^2SZ) at 30 GHz up to about 3 μK (pqiCMB) and 13 μK (pβ_t^2SZ) at 675 GHz. The high magnitudes of both signals at high frequencies may allow its detection with the next generation of submillimeter instruments.

The analysis of the evolution with the redshift, was made from simulations of 61 contiguous boxes, each with a comoving depth of $100\,h^{-1}$ Mpc, with redshifts ranging from $z \simeq 0.034$ to $z \simeq 7.24$. The results clearly show that in each redshift, both effects follow the local distribution of the gas. In the case of pqiCMB, because the primary CMB quadrupole is nearly constant, the polarization pattern follows mostly the gas column densities. In the case of pβ_t^2SZ, because the column densities are weighted by the square of the transverse velocity of the gas, the polarization pattern shows structures enhanced or dimmed from the background, depending on their internal velocity structure. This last effect can bring strong consequences for the results of the integration of the signal up to high redshifts along the light cone, which can considerably degrade the imprint of individual structures due to the overlap of signals along the LOS.

The redshift distribution of the polarization degrees shows that the contribution for the polarization signal is highest at $z \simeq 1$ and $z \simeq 0.5$ for the pqiCMB and pβ_t^2SZ, respectively. We also note that only about 7% of the total signal comes from $z > 4$ for the former and $z > 3$ for the latter and both signals converge rapidly above these redshifts.

From the polarization angular power spectra is also clear that both effects show similar shapes and the power of the kinematic component is 100 times smaller than the induced quadrupole signal. The maxima of about 10^{-5} μK^2 (pqiCMB) and 10^{-7} μK^2 (pβ_t^2SZ) are achieved roughly at $\ell \sim 25{,}000$. At small angular scales, these secondary polarization effects will dominate over the primordial modes and although the power of the gravitational lensing is larger than the peak of the scattering induced polarization signals, at high multipoles of about $\ell \sim 40{,}000$ the pqiCMB may become the prominent contribution.

With the expected improvement in sensitivity and angular resolution of the next generation sub/millimeter and multi-frequency instruments, measurements of the CMB induced polarization by galaxy clusters may become feasible and bring crucial information to better understand the underlying parameters that describe our universe. For instance, the evolution with the redshift of the quadrupole signal can be done from cluster polarization signals to establish the integrated Sachs–Wolfe effect and therefore the equation of state of dark energy. This powerful method was mentioned previously by Cooray & Baumann (2003, and references therein) and would be explored in a subsequent study. The spectral signature of the pβ_t^2SZ is also the added value for its detection and separation from other signals with multi-frequency measurements, and therefore a valuable method to infer the transverse velocity of galaxy clusters.

E.P.R.G.R. is supported by grant POPH-QREN-SFRH/BD/45613/2008, from FCT (Portugal), G.-C.L. is supported by NSC Grant 100-2112-M-032-001-MY3 and A.J.C.d.S. is supported by a Ciência 2007 contract, funded by FCT/MCTES (Portugal) and POPH/FSE (EC). E.P.R.G.R. and A.J.C.d.S. acknowledge financial support from project FCOMP-01-0124-FEDER-015309 and PTDC/FIS/111725/2009, from FCT (Portugal). The hydrodynamic simulations were run with the CAUP's EXO computer.

APPENDIX

ANGULAR POWER SPECTRUM COMPUTATION

Since Q and U depend on the coordinate system, it is more convenient to work with maps of the scalar E and pseudo-scalar B-modes, which are reference-frame independent quantities. In terms of parity transformation, E remains unchanged but the sign of B changes in analogy with the electric and magnetic fields, respectively (e.g., Zaldarriaga & Seljak 1997; Kamionkowski et al. 1997; Zaldarriaga 1998). Using the relations (9) and (10), and the linear combination between $a_{\pm 2,lm}$, E, and B can be defined as

$$E(\hat{n}) = \sum_{\ell} \sum_{m} a_{E,\ell m} Y_{\ell m}(\hat{n}) \tag{A1}$$

$$B(\hat{n}) = \sum_{\ell} \sum_{m} a_{B,\ell m} Y_{\ell m}(\hat{n}) \tag{A2}$$

with $a_{E,\ell m} = -(a_{2,\ell m}+a_{-2,lm})/2$ and $a_{B,\ell m} = \mathrm{i}(a_{2,\ell m}-a_{-2,\ell m})/2$. For small sky patches, Q_T and U_T can be decomposed in the Fourier domain as

$$Q_T(\boldsymbol{\theta}) = \frac{1}{(2\pi)^2}\int [E(\boldsymbol{\ell})\cos(2\alpha) - B(\boldsymbol{\ell})\sin(2\alpha)]e^{i\boldsymbol{\ell}.\boldsymbol{\theta}}d^2\boldsymbol{\ell} \tag{A3}$$

$$U_T(\boldsymbol{\theta}) = \frac{1}{(2\pi)^2}\int [E(\boldsymbol{\ell})\sin(2\alpha) + B(\boldsymbol{\ell})\cos(2\alpha)]e^{i\boldsymbol{\ell}.\boldsymbol{\theta}}d^2\boldsymbol{\ell}, \tag{A4}$$

where α is the angle between the mode $\boldsymbol{\ell}$ and the Fourier plane. The power spectra of the E- and B-modes can be computed directly in the Fourier space by preforming the Fourier transform (FT) of the previous relations, resulting in

$$E(\boldsymbol{\ell}) = \int [\tilde{Q}_T\cos(2\alpha) + \tilde{U}_T\sin(2\alpha)]e^{-i\boldsymbol{\ell}.\boldsymbol{\theta}}d^2\boldsymbol{\theta} \tag{A5}$$

$$B(\boldsymbol{\ell}) = \int [-\tilde{Q}_T\sin(2\alpha) + \tilde{U}_T\cos(2\alpha)]e^{-i\boldsymbol{\ell}.\boldsymbol{\theta}}d^2\boldsymbol{\theta} \tag{A6}$$

with $\tilde{Q}_T = \mathrm{FT}(Q_T(\boldsymbol{\theta}))$ and $\tilde{U}_T = \mathrm{FT}(U_T(\boldsymbol{\theta}))$. Applying Fourier transforms to these equations, we obtain maps of the E- and B-modes in real space.

Given the small areas of our sky realizations, the flat sky approximation presented above is a good approximation to compute the E and B angular power spectra in our maps. The power is computed in Fourier space using Equations (A5) and (A6) and assuming concentric shells, with a fixed width in logarithmic scale, from the fundamental mode up to the Nyquist frequency (da Silva et al. 2001b; da Silva 2002).

REFERENCES

Amblard, A., & White, M. 2005, New Astron., 10, 417
Audit, E., & Simmons, F. L. 1999, MNRAS, 305, L27
Baumann, D., & Cooray, A. 2003, New Astron. Rev., 47, 839
Baumann, D., Cooray, A., & Kamionkowski, M. 2003, New Astron., 8, 565
Bennett, C. L., Halpern, M., Hinshaw, G., et al. 2003, ApJS, 148, 1
Bunn, E. F. 2006, Phys. Rev. D, 73, 123517
Challinor, A. D., Ford, M. T., & Lasenby, A. N. 2000, MNRAS, 312, 159
Cooray, A., & Baumann, D. 2003, Phys. Rev. D, 67, 063505
Cooray, A., Huterer, D., & Baumann, D. 2004, Phys. Rev. D, 69, 027301
Cooray, A., Melchiorri, A., & Silk, J. 2003, Phys. Lett. B, 554, 1
Couchman, H. M. P., Thomas, P. A., & Pearce, F. R. 1995, ApJ, 452, 797
da Silva, A. 2002, PhD thesis, Univ. Sussex
da Silva, A., Barbosa, D., Liddle, A. R., & Thomas, P. A. 2000, MNRAS, 317, 37
da Silva, A. C., Barbosa, D., Liddle, A. R., & Thomas, P. A. 2001a, MNRAS, 326, 155
da Silva, A. C., Kay, S. T., Liddle, A. R., et al. 2001b, ApJ, 561, L15
Diego, J. M., Mazzotta, P., & Silk, J. 2003, ApJ, 597, L1
Holder, G. P., & Loeb, A. 2004, ApJ, 602, 659
Itoh, N., Nozawa, S., & Kohyama, Y. 2000, ApJ, 533, 588
Kamionkowski, M., Kosowsky, A., & Stebbins, A. 1997, Phys. Rev. D, 55, 7368
Kamionkowski, M., & Loeb, A. 1997, Phys. Rev. D, 56, 4511
Kosowsky, A. 1996, Ann. Phys., 246, 49
Lavaux, G., Diego, J. M., Mathias, H., & Silk, J. 2004, MNRAS, 347, 729
Leroy, J.-L. 2000, Polarization of Light and Astronomical Observation (Amsterdam: Gordon and Breach)
Lewis, A., Challinor, A., & Lasenby, A. 2000, ApJ, 538, 473
Liu, G.-C., da Silva, A., & Aghanim, N. 2005, ApJ, 621, 15
Ma, C., & Bertschinger, E. 1995, ApJ, 455, 7
Portsmouth, J. 2004, Phys. Rev. D, 70, 063504
Sazonov, S. Y., & Sunyaev, R. A. 1999, MNRAS, 310, 765
Seljak, U., & Zaldarriaga, M. 1996, ApJ, 469, 437
Seto, N., & Sasaki, M. 2000, Phys. Rev. D, 62, 123004
Shimon, M., Rephaeli, Y., O'Shea, B. W., & Norman, M. L. 2006, MNRAS, 368, 511
Shimon, M., Rephaeli, Y., Sadeh, S., & Keating, B. 2009, MNRAS, 399, 2088
Smoot, G. F., Bennett, C. L., Kogut, A., et al. 1992, ApJ, 396, L1
Springel, V. 2005, MNRAS, 364, 1105
Sunyaev, R. A. 1982, Sov. Astron. Lett., 8, 175
Sunyaev, R. A., & Zel'dovich, Y. B. 1970, Ap&SS, 7, 3
Sunyaev, R. A., & Zel'dovich, Y. B. 1972, Comments Astrophys. Space Phys., 4, 173
Sunyaev, R. A., & Zel'dovich, Y. B. 1980, MNRAS, 190, 413
Sunyaev, R. A., & Zel'dovich, Y. B. 1981, Sov. Sci. Rev. E: Astrophys. Space Phys. Rev., 1, 1
Zaldarriaga, M. 1998, PhD thesis, Massachusetts Institute of Technology
Zaldarriaga, M., & Seljak, U. 1997, Phys. Rev. D, 55, 1830
Zel'dovich, Y. B., & Sunyaev, R. A. 1980, Sov. Astron. Lett., 6, 285